



This is a repository copy of *Comparative study of the giant stress impedance behavior of commercial amorphous ribbons for strain sensing applications*.

White Rose Research Online URL for this paper:
<https://eprints.whiterose.ac.uk/188026/>

Version: Published Version

Article:

Pan, P. and Hayward, T.J. (2022) Comparative study of the giant stress impedance behavior of commercial amorphous ribbons for strain sensing applications. *Journal of Applied Physics*, 131 (21). 214503. ISSN 0021-8979

<https://doi.org/10.1063/5.0088988>

Reuse

This article is distributed under the terms of the Creative Commons Attribution (CC BY) licence. This licence allows you to distribute, remix, tweak, and build upon the work, even commercially, as long as you credit the authors for the original work. More information and the full terms of the licence here:
<https://creativecommons.org/licenses/>

Takedown

If you consider content in White Rose Research Online to be in breach of UK law, please notify us by emailing eprints@whiterose.ac.uk including the URL of the record and the reason for the withdrawal request.



eprints@whiterose.ac.uk
<https://eprints.whiterose.ac.uk/>

Comparative study of the giant stress impedance behavior of commercial amorphous ribbons for strain sensing applications

Cite as: J. Appl. Phys. **131**, 214503 (2022); <https://doi.org/10.1063/5.0088988>

Submitted: 21 February 2022 • Accepted: 04 May 2022 • Published Online: 02 June 2022

Published open access through an agreement with JISC Collections

 Patrick Pan and T. J. Hayward



View Online



Export Citation



CrossMark

ARTICLES YOU MAY BE INTERESTED IN

[Via-based miniaturized rasorber using graphene films](#)

Journal of Applied Physics **131**, 214504 (2022); <https://doi.org/10.1063/5.0091654>

[Plasma enhanced chemical vapor deposition of p-type Cu₂O from metal organic precursors](#)

Journal of Applied Physics **131**, 215301 (2022); <https://doi.org/10.1063/5.0089757>

[Formation of voids and their role in the recovery of sputtered AlN during high-temperature annealing](#)

Journal of Applied Physics **131**, 215304 (2022); <https://doi.org/10.1063/5.0088948>

Journal of Applied Physics **Special Topics** Open for Submissions [Learn More](#)

Comparative study of the giant stress impedance behavior of commercial amorphous ribbons for strain sensing applications

Cite as: J. Appl. Phys. 131, 214503 (2022); doi: 10.1063/5.0088988

Submitted: 21 February 2022 · Accepted: 4 May 2022 ·

Published Online: 2 June 2022



Patrick Pan^{a)}  and T. J. Hayward

AFFILIATIONS

Department of Materials Science and Engineering, The University of Sheffield, Sheffield, United Kingdom

^{a)}Author to whom correspondence should be addressed: ppan4@sheffield.ac.uk

ABSTRACT

The giant magnetoimpedance (GMI) and giant stress impedance (GSI) behaviors of amorphous ribbons composed of three commercially available materials ($\text{Co}_{66}\text{Si}_{15}\text{B}_{14}\text{Fe}_4\text{Ni}_1$, $\text{Fe}_{81}\text{B}_{13}\text{Si}_{3.5}\text{C}_2$, and $\text{Ni}_{40}\text{Fe}_{40}\text{Si} + \text{B}_{19}\text{Mo}_{1-2}$) with differing saturation magnetostriction constants (λ_s) and Young's moduli (E) were studied under longitudinal stress/strain. The linearity of the ribbons' GSI responses and gauge factors was measured to create a figure of merit and compare their stress/strain sensing performance for strains up to $\varepsilon = 10 \times 10^{-3}$. We observed that the $\text{Ni}_{40}\text{Fe}_{40}\text{Si} + \text{B}_{19}\text{Mo}_{1-2}$ ribbon displayed the best performance for low strains ($\varepsilon < 1 \times 10^{-3}$), whereas the $\text{Co}_{66}\text{Si}_{15}\text{B}_{14}\text{Fe}_4\text{Ni}_1$ ribbon displayed the best performance for higher strains ($\varepsilon < 10 \times 10^{-3}$). We conclude that the suitability of a material for sensing strains in any given strain regime has a complex dependence on both λ_s and E , the former of which dictates both the absolute magnitude of the impedance variation materials exhibit (i.e., the dynamic range), while both λ_s and E control how their impedances vary with applied strain.

© 2022 Author(s). All article content, except where otherwise noted, is licensed under a Creative Commons Attribution (CC BY) license (<http://creativecommons.org/licenses/by/4.0/>). <https://doi.org/10.1063/5.0088988>

I. INTRODUCTION

The giant magnetoimpedance (GMI) effect has been studied extensively for use in technological applications.¹⁻³ The GMI effect is defined as the variation in absolute impedance, Z , of a ferromagnetic conductor when subjected to DC magnetic fields a DC magnetic field. Its magnitude usually peaks at low MHz frequencies, typically under $f = 10$ MHz,^{3,4} where it results from variation in the skin depth (δ) of the electrical current with the magnetic field. The effect can be understood from classical electrodynamic theory, in which the skin depth may be expressed as $\delta = \sqrt{\frac{\rho}{\pi f \mu}}$ where f is the frequency of the electrical current, μ is the transverse magnetic permeability of the conductor, and ρ is the resistivity of the conductor.^{3,4} Here, applying magnetic fields changes the value of μ , resulting in variation of the skin depth and, thus, Z with the applied field. GMI ratios can be as large as several hundred percent when the microstructure and domain structure of the (typically amorphous) materials are optimized to produce high values of μ .⁵⁻⁷ Harnessing these phenomena can allow the creation of a highly sensitive magnetic field sensor^{4,8} with

promising applications in biosensing technologies.⁹⁻¹² Furthermore, other external stimuli can also affect μ , allowing the design of highly sensitive GMI sensors for detecting, e.g., temperature^{13,14} and externally applied stresses/strains.^{2,15,16}

In sensing applications, it is desirable to simply measure how the impedance of a ferromagnetic conductor varies with the target stimuli, rather than to perform full, field-swept GMI measurements in the presence of the stimuli. Such an approach was first reported in 1997 by Shen *et al.* who observed a direct correlation between applied stress and impedance in CoSiB amorphous wires,¹⁷ a phenomenon known as the giant stress impedance (GSI) effect. Since then, there have been many studies investigating the GSI effect in wires¹⁸⁻²¹ and ribbons²²⁻²⁴ with a common understanding that the GSI effect results from the variation of μ with stress/strain due to magnetoelastic effects.

Recently, we reported on the GMI behavior of three commercialized amorphous ribbons with differing magnetic properties, including the saturation magnetostriction coefficient, λ_s .²⁵ It is widely agreed that λ_s determines the magnitude of the GMI response of a material, with lower λ_s coefficients resulting in higher

GMI ratios. This is because materials with near-zero (or negative) λ_s coefficients have higher transverse permeabilities.^{4,26–28} Our results supported this view, with a $\text{Co}_{66}\text{Si}_{15}\text{B}_{14}\text{Fe}_4\text{Ni}_1$ ribbon with near-zero λ_s producing a much larger GMI response than the other materials studied. However, the situation for the GSI effect is more complex with λ_s not only affecting μ , but also how sensitive a material's magnetic properties are to changes in applied stress, and, in combination with a material's mechanical properties, how sensitive they are to applied strain. It is, therefore, unclear how λ_s should be optimized for any given stress/strain sensing application.

In this study, we have investigated correlations between the GSI effect, GMI effect, and λ_s in amorphous ribbons composed of three commercially available materials and assessed their applicability to strain sensing applications. Our results show that selecting materials with low λ_s will maximize both the GMI and GSI ratios. However, choosing a material for a given strain sensing application is more complex, with the best choice of material depending strongly on the range of stresses/strains that need to be sensed.

II. EXPERIMENTAL METHOD

A. Sample preparation

Three bulk amorphous foils were purchased from Goodfellow. The foils all had thicknesses of $25\ \mu\text{m}$, but different chemical compositions: $\text{Co}_{66}\text{Si}_{15}\text{B}_{14}\text{Fe}_4\text{Ni}_1$, $\text{Fe}_{81}\text{B}_{13}\text{Si}_{3.5}\text{C}_2$, and $\text{Ni}_{40}\text{Fe}_{40}\text{Si} + \text{B}_{19}\text{Mo}_{1-2}$. These three materials were chosen for the study due to each having different values of λ_s , as shown in Table I. For brevity, the ribbon samples will be referred to as Co-rich ($\text{Co}_{66}\text{Si}_{15}\text{B}_{14}\text{Fe}_4\text{Ni}_1$), Fe-rich ($\text{Fe}_{81}\text{B}_{13}\text{Si}_{3.5}\text{C}_2$), and Ni-rich ($\text{Ni}_{40}\text{Fe}_{40}\text{Si} + \text{B}_{19}\text{Mo}_{1-2}$), respectively.

In Ref. 25, we performed the basic characterization of the structural properties of all three materials to confirm the material properties quoted by the supplier. X-ray diffraction (XRD) measurements with Cu $K\alpha$ radiation affirmed the amorphous crystal structure of all three materials with the single broad peak being observed at $2\theta \sim 45^\circ$. In addition, each of the materials surface roughness was measured using Atomic Force Microscopy (AFM), with root mean square surface roughness (R_q) 4.15, 15.3, and 14.8 nm being observed for Co-rich, Fe-rich, and Ni-rich foils, respectively.

The three materials' (with common dimensions of $10\ \text{mm} \times 2\ \text{mm} \times 25\ \mu\text{m}$) hysteresis loops were measured at room temperature using a superconducting quantum interference device (SQUID) [Fig. 1(a)].²⁵ Of the three samples, the Co-rich sample exhibited the highest susceptibility when compared to the other two ribbon samples. Figure 1(b) presents the coercive fields (H_C) of

all three samples with values of 0.01, 0.16, and 0.23 Oe of the observed Co-rich, Fe-rich, and Ni-rich foils, respectively.

In this study, two sets of ribbons composed of the three materials with common cross sections of $10\ \text{mm} \times 25\ \mu\text{m}$ were prepared by mechanically cutting the foils. The first set of samples (batch 1) had lengths of 120 mm, while the second set of samples (batch 2) had lengths of 200 mm. The sample lengths batch 2 samples were chosen to give the ribbons an aspect ratio (l/w) of 20 where it was expected that GMI/GSI ratios would be maximized.²⁵ The shorter length of the batch 1 samples was chosen to allow uniform magnetic fields to be applied to them using a Helmholtz coil.

B. GMI and GSI measurements

Batch 1 samples were used to study the variation of the samples GMI under stress/strain. The ribbons were placed inside a Helmholtz coil with a uniform field region of $\sim 150\ \text{mm}$ long and a maximum field strength of $H_{\text{DC}} = \pm 150\ \text{Oe}$. The ends of the sample were clamped to a manual tensile test stand (Mark-10 Model ES-30) (Fig. 2). Applied forces were measured using a force gauge (Mark—10 Series 5), and the applied longitudinal tensile stresses were calculated using the equation $\sigma = F/A$, where F was the applied tensile force and A was the ribbons' cross-sectional area. The samples' tensile strains were calculated using the equation $\varepsilon = \sigma/E$, using the values of E listed in Table I.

The ribbons' impedances were measured in the range 0.1–10 MHz by connecting them to an impedance analyzer (Agilent 4294A) using a four-terminal (4T) connection. Parasitic impedances from the test fixture and test leads were compensated using an open, short, and load calibration methodology. We note that parasitic impedances at the connection between the test leads and the sample were not accounted for in our de-embedding procedure. However, as we showed in a previous study, these effects are relatively minor and are not expected to substantially affect our measurements.²⁵

GMI measurements under induced stress/strain were performed by measuring the samples' impedance spectra while sweeping the applied field between -150 and $+150\ \text{Oe}$ and applying constant longitudinal stresses of either 0 or 40 MPa. At both stresses, the ribbons' GMI ratios were then calculated using the expression

$$\text{GMI} = \frac{|Z(H)| - |Z(H_{\text{max}})|}{|Z(H_{\text{max}})|} \times 100\%, \quad (1)$$

where $Z(H_{\text{max}})$ is the absolute impedance measured at the highest field ($H_{\text{DC}} = \pm 150\ \text{Oe}$) and $Z(H)$ is the absolute impedance measured at field H . The peak GMI ratio (i.e., the highest magnitude GMI

TABLE I. Magnetic and mechanical properties for $\text{Co}_{66}\text{Si}_{15}\text{B}_{14}\text{Fe}_4\text{Ni}_1$, $\text{Fe}_{81}\text{B}_{13}\text{Si}_{3.5}\text{C}_2$, and $\text{Ni}_{40}\text{Fe}_{40}\text{Si} + \text{B}_{19}\text{Mo}_{1-2}$ ribbons, as quoted by the supplier.^{29–31}

Ribbon sample	Magnetic properties		Mechanical properties Young's modulus (GPa)
	Magnetostriction coefficient λ_s (ppm)	Saturation flux density (T)	
$\text{Co}_{66}\text{Si}_{15}\text{B}_{14}\text{Fe}_4\text{Ni}_1$ (Co-rich)	<1	0.55	58
$\text{Fe}_{81}\text{B}_{13}\text{Si}_{3.5}\text{C}_2$ (Fe-rich)	30	1.6	61
$\text{Ni}_{40}\text{Fe}_{40}\text{Si} + \text{B}_{19}\text{Mo}_{1-2}$ (Ni-rich)	8	0.8	150

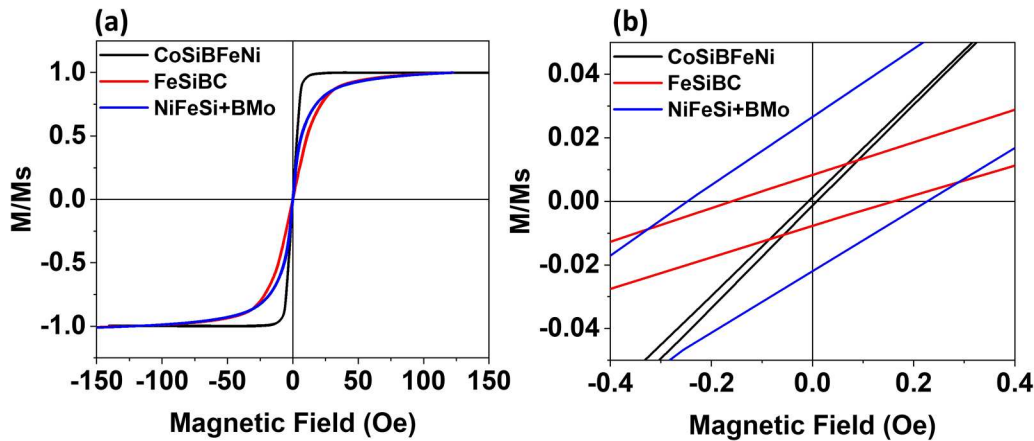


FIG. 1. (a) Normalized M-H hysteresis loops of Co-rich, Fe-rich, and Ni-rich samples with common dimensions of $10\text{ mm} \times 2\text{ mm} \times 25\text{ }\mu\text{m}$. (b) A more detailed image of the center of the loops to enable each sample's coercive fields (H_c) to be seen. The applied field was parallel to the ribbon axis.

ratio), at both stresses, was obtained either at $H = 0\text{ Oe}$ for samples that displayed single-peak GMI curve or at a positive/negative finite value of H for samples that displayed a double-peak GMI curve.

Batch 2 samples were used to characterize the ribbons' GSI behaviors. The ribbons were mounted in the same way as in Fig. 2; however, no fields were applied by the Helmholtz coil. The impedance spectra of each ribbon were measured under applied stresses up to 600 MPa. GSI ratios were calculated using the expression²²

$$\text{GSI} = \frac{|Z(\sigma)| - |Z(0)|}{|Z(0)|} \times 100\%, \quad (2)$$

where $Z(\sigma)$ is the absolute impedance at stress σ and $Z(0)$ is the absolute impedance measured at zero applied stress. The peak GSI ratio (the highest magnitude GSI ratio) was obtained either at finite values of σ or at the largest value of stress applied (σ_{max}) for samples that showed a monotonic trend of GSI with σ .

In order to analyze how the GSI behavior of the ribbons could be optimized for strain sensing applications, two factors were considered: the linearity of the ribbons' GSI responses and their average strain sensitivities ($\Delta\text{GSI}/\Delta\varepsilon$), also known as the gauge factor (GF). Both were calculated for each applied strain $\varepsilon(\sigma_i)$ by considering the GSI response over a strain range between $\varepsilon = 0$ and $\varepsilon(\sigma_i)$. The gauge factor for measurement up to strain value $\varepsilon(\sigma_i)$ was, thus, calculated using $GF(\sigma_i) = \text{GSI}(\sigma_i)/\varepsilon(\sigma_i)$. To characterize the linearity of the ribbons' GSI, we performed a linear regression of the GSI data between $\varepsilon = 0$ and $\varepsilon(\sigma_i)$, and calculated the value of R^2 to judge the quality of the linear fit. From these two values, we created a normalized figure of merit (FoM) in the range 0–1 to allow comparison between the differing responses of the three materials,

$$\text{FoM} = R^2 \times \left(\frac{\text{GF}}{\text{GF}_{max}} \right), \quad (3)$$

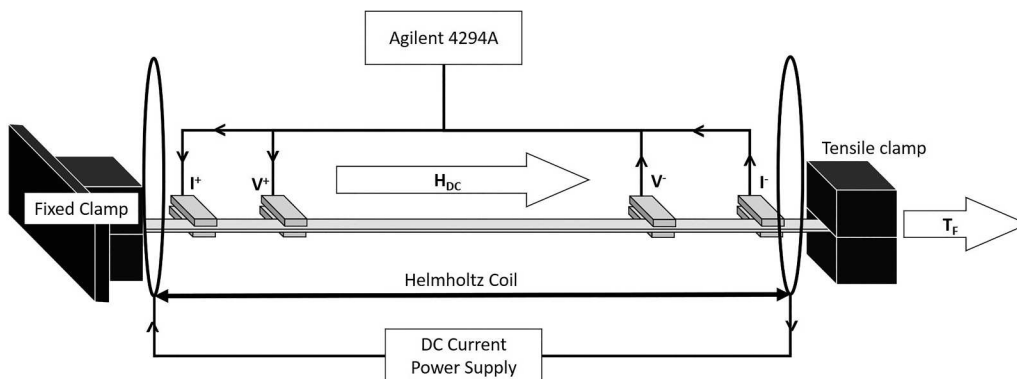


FIG. 2. Schematic diagram of the experimental setup used to perform GMI measurements under tensile stress/strain.

where the $G_{F_{max}}$ was the largest gauge factor measured across all the samples, to allow direct comparisons between FOM for different materials. Thus, the higher the FOM value the better a sample's performance as a sensor was for a strain within a range bounded by ϵ_i .

III. RESULTS AND DISCUSSION

A. Influence of tensile stress/strain on GMI behavior

Figure 3 presents GMI data as a function of applied field (H) for all three samples at their respective critical frequencies (f_0), i.e., the frequency at which their peak GMI ratios were maximized. The Co-rich sample exhibited the highest GMI ratio (71.6%), followed by Fe-rich (14.6%) and Ni-rich (14.2%) samples. The difference in the GMI responses correlated to the ribbons differing λ_s coefficients, with the near-zero λ_s coefficient of the Co-rich ribbon produced a larger peak GMI response than the Fe-rich and Ni-rich ribbons, which had larger positive λ_s . This was consistent with the previously published literature, where materials with negative and near-zero λ_s produced larger GMI responses than materials with positive λ_s .^{4,28,32} In addition, the GMI responses of all three samples were consistent with their magnetic properties with the hierarchy of coercive fields being the inverse of the hierarchy of GMI ratios (i.e., softer materials exhibited higher GMI ratios). The surface topography of the Co-rich sample may also have contributed to its high peak GMI ratio since it had much lower surface roughness than the other two materials. Surface roughness has previously been shown to be inversely correlated with GMI ratios in experimental studies.^{33,34}

Figure 4 presents the three samples' peak GMI ratios as a function of frequency. For all samples, the peak GMI ratio was reached at $f_0 = 1\text{--}2$ MHz and then decreased as the frequency was increased further. The GMI ratio peaked at different f_0 for each sample; 1.3 MHz (Co-rich), 1.4 MHz (Fe-rich), and 1.7 MHz (Ni-rich). The frequency variation of the peak GMI ratio could be attributed to changes in the magnetization dynamics that contributed to the ribbons' transverse permeabilities. At lower frequencies,

both domain wall motion and magnetization rotation contributed; however, at frequencies higher than f_0 , the domain wall motion was damped by eddy currents and so magnetization rotation alone contributed to the transverse permeability (μ), resulting in a decrease in the GMI ratio.^{3,4}

Figures 3 and 4 also present GMI curves measured at f_0 under $\sigma = 40$ MPa of tensile stress. Under stress, the peak GMI ratios of all three samples decreased, but each with varying amounts as listed in Table II. Furthermore, the GMI curve for the Co-rich sample changed from a single-peak to a double-peak form, indicating a change in the direction and strength of the anisotropy field within the sample.^{35–37} The Fe- and Ni-rich samples exhibited single-peak GMI curves at both $\sigma = 0$ and $\sigma = 40$ MPa.

Figure 4 illustrates how the observed reduction of peak GMI ratios by applied stress extended to all the frequencies studied. This suppression of the GMI ratio occurred due to the creation of additional magnetoelastic anisotropies that decreased the peak value of μ , thus increasing the minimum skin depth and the maximum value of impedance that the materials exhibited. One might, therefore, expect materials with larger λ_s to show greater sensitivity to stress/strain. Indeed, at the first glance, the degree to which GMI ratios were suppressed from their initial values appeared correlated with the size of the materials λ_s coefficients, with the Fe-rich ribbons, which had the largest value of λ_s , showing a much larger *proportional* decrease in the GMI ratio than the Co-rich ribbon, which had the smallest λ_s . Furthermore, the degree to which the peak GMI ratios were suppressed from their initial values correlated with the size of the materials λ_s coefficient, with the Fe-rich ribbons, having the largest value of λ_s , showing a much larger decrease in the GMI ratio than the Co-rich ribbon. However, closer examination of the data presented evidence of a more complicated picture. For example, at $H = 0$ Oe [Fig. 5(a)], the change in the GMI ratio of the Co-rich ribbon was much larger than the other two materials exhibited at any applied field, with an absolute stress-induced GMI ratio change of 15.7% (Fe-rich ribbon peak: 9.9%, Ni-rich ribbon peak: 3.8%) [see the inset of Fig. 3(a)].

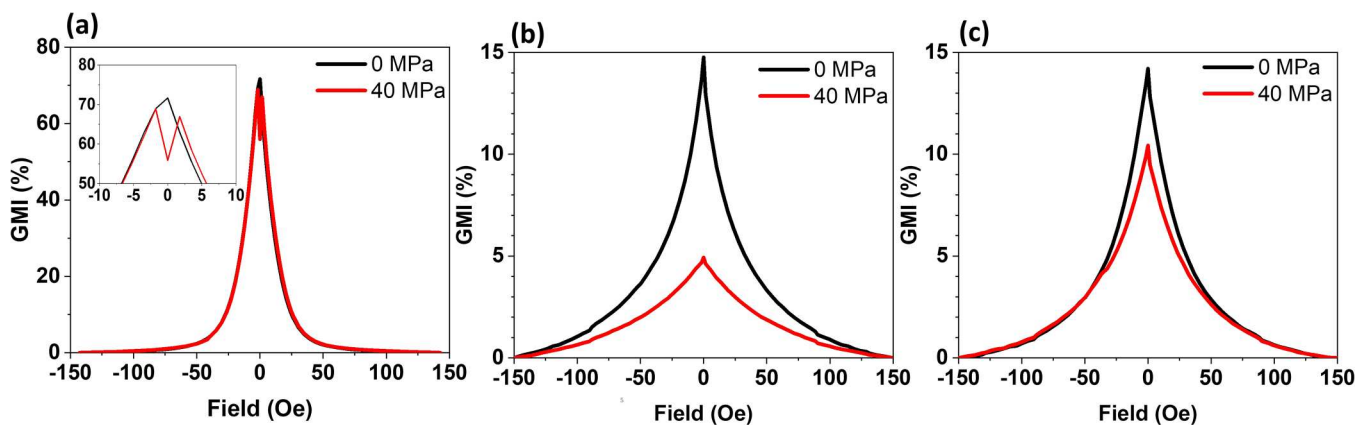


FIG. 3. GMI data measured for (a) Co-rich, (b) Fe-rich, and (c) Ni-rich ribbon samples at their respective f_0 : 1.3, 1.4, and 1.7 MHz. Data are shown for tensile stresses of 0 MPa (black lines) and 40 MPa (red lines).

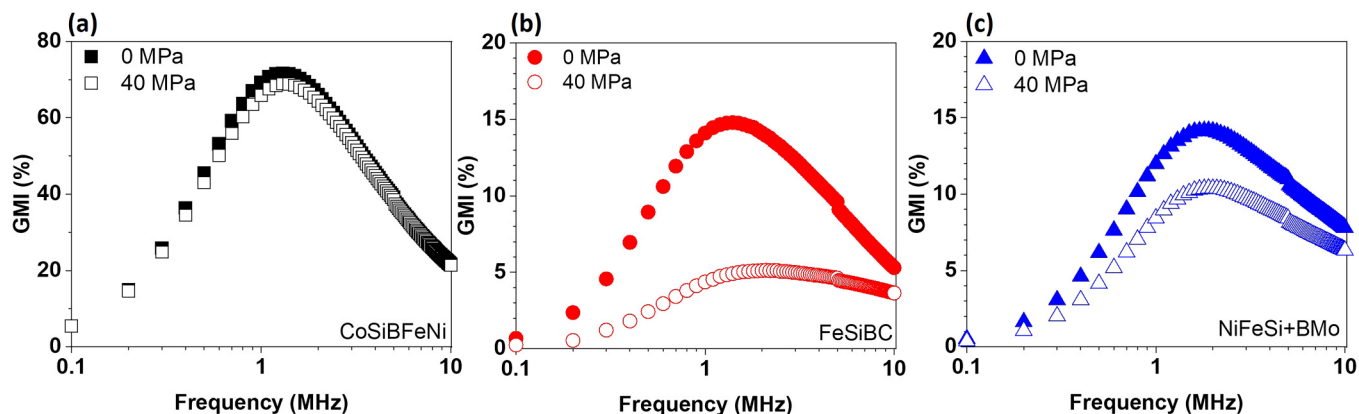


FIG. 4. Frequency dependence of peak GMI ratios for (a) Co-rich, (b) Fe-rich, and (c) Ni-rich ribbon samples under tensile stresses of 0 (measured at $H = 0$ Oe for all samples) and 40 MPa (measured at $H = \pm 1.7$ Oe for Co-rich sample and $H = 0$ Oe for Fe- and Ni-rich samples).

These data illustrate the conflicting considerations of materials selection for a stress/strain sensor: while the Fe- and Ni-rich ribbons with large λ_s clearly showed larger changes in their peak GMI ratios than the Co-rich ribbon, at zero field the Co-rich ribbon sample displayed an even larger effect, despite its low λ_s . This can be understood as follows: the size of a ribbon's GMI response is defined by the difference in its skin depth at the point where magnetic permeability is maximized, and the point where a strong applied field almost entirely suppresses the permeability. For ribbons with near-zero (or negative) λ_s , the difference in skin depth is large, and these materials have a large range of impedance values they can potentially exhibit, but these would be expected to vary relatively slowly with additional stress/strain, as induced anisotropies will be weak. For ribbons with a higher λ_s , the range of available impedance values is more limited (as the maximum permeability observed is lower due to pre-existing magnetoelastic anisotropies), but variation with applied stress would be expected to be more rapid and dramatic. Out of the studied materials, at this single stress value, the dominating factor was clearly the total range of available impedance values; hence, the Co-rich ribbon with its large dynamic range produced the largest absolute change in the GMI ratio on the application of stress.

A further interesting observation for the Co-rich ribbon (measured at $H = 0$ Oe) was that at frequencies in the range $f < 0.3$ MHz the sample displayed a slightly higher GMI ratio (by $\sim 1.5\%$ – 2%) at

$\sigma = 40$ MPa than it did at $\sigma = 0$ MPa (Fig. 5). This was counter to expectations, as additional anisotropies are typically expected to reduce the permeability and, thus, increase skin depth. However, at these low frequencies, the addition of a weak magnetoelastic anisotropy aided the magnetization dynamics, resulting in an increased permeability and reduced skin depth. At higher frequencies, GMI was always decreased by the application of stress. This suggested that the additional anisotropy increased domain wall mobility within the ribbons, but did not similarly assist magnetization rotation, as typically the former mechanism dominates over the latter at lower frequencies.^{22,38} Comparatively, Fe- and Ni-rich ribbon samples displayed a monotonic trend at all frequencies between both stresses, which suggests that the magnetoelastic anisotropy only reduced the transverse permeability of these samples. These results suggested a further complication in materials selection for strain sensing; clearly, the addition of stronger magnetoelastic anisotropies would eventually result in decreases in GMI for all materials; thus, it was likely that the Co-rich ribbon exhibited a non-monotonic variation of GMI with stress at some frequencies, a highly undesirable property for a sensor. Such behaviors are discussed in more detail in Secs. III B and III C.

B. GSI behavior

Having characterized the GMI behavior of the samples under stress, we turned our attention to characterizing their GSI behavior

TABLE II. Maximum GMI ratio of each sample before and after applied stress, and the stress-induced change in the GMI ratios. The ribbons' magnetostriction coefficients λ_s are also shown.

Ribbon sample	λ_s (ppm)	GMI behavior		
		Peak GMI ratio ($\sigma = 0$ MPa) (%)	Peak GMI ratio ($\sigma = 40$ MPa) (%)	Stress-induced change in GMI ratio (%)
Co-rich	<1	71.6	68.9	2.5
Fe-rich	30	14.8	4.9	9.9
Ni-rich	8	14.2	10.4	3.8

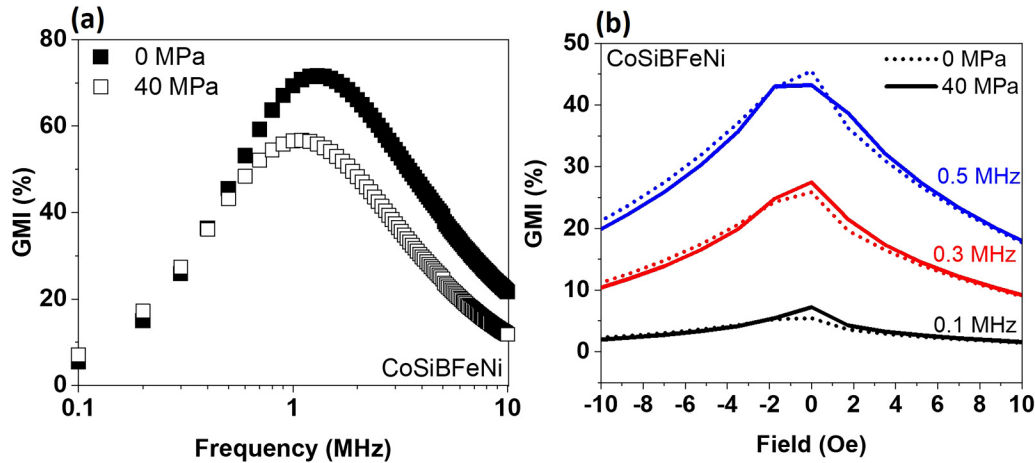


FIG. 5. The GMI ratio of the Co-rich ribbon sample with respect to (a) frequency (measured at $H=0$ Oe) and (b) field (at frequencies of 0.1, 0.3, and 0.5 MHz).

in the absence of applied field. Figure 6 presents exemplar GSI behavior curves measured from the three materials at $f=0.3$ MHz [Fig. 6(a)] and $f=2$ MHz [Fig. 5(b)] under tensile stresses up to $\sigma=600$ MPa. At both frequencies, the Fe- and Ni-rich samples exhibited monotonic behaviors, where GSI ratios were negative and consistently decreased as the stress increased, with the Fe-rich ribbon consistently exhibiting higher GSI ratios than the Ni-rich ribbon. In contrast, the GSI curves for the Co-rich sample exhibited two distinct behaviors: at $f=0.3$ MHz [Fig. 6(a)], positive GSI ratios were observed for stresses under $\sigma=150$ MPa. These peaked at 50 MPa ($\sim 3.3\%$) and then decreased monotonically for higher stresses. This behavior was equivalent to that observed in the GMI data at low frequencies. At $f=2$ MHz, a different behavior was observed. For stress up to $\sigma=200$ MPa, the data were like the Fe- and Ni-rich samples, with a monotonic trend and negative

GSI ratios. However, beyond $\sigma=200$ MPa, the sample's GSI ratios decreased again, before tending toward a constant value as the stress approached $\sigma=600$ MPa. The peak GSI ratios of the Co-rich ribbon were universally higher than those of the Fe-rich and Ni-rich ribbons.

Figure 7 presents frequency-dependent GSI ratios of the three materials for $\sigma=0$ –600 MPa and $f=0.1$ –10 MHz. Like the GMI behavior, the GSI behavior exhibited a critical frequency, f_0 , where the sample's highest peak GSI ratio was observed; this was 2.5 MHz for Co-rich and 1.5 MHz for Fe- and Ni-rich samples. The maximum peak GSI ratio was observed in the Co-rich ribbon (-18.3%), followed by the Fe-rich (-10.8%) and Ni-rich (-6.8%) ribbons. This indicated that the peak GSI behaved in a similar manner to the peak GMI ratios, with both ultimately being determined by the maximum possible transverse permeability available

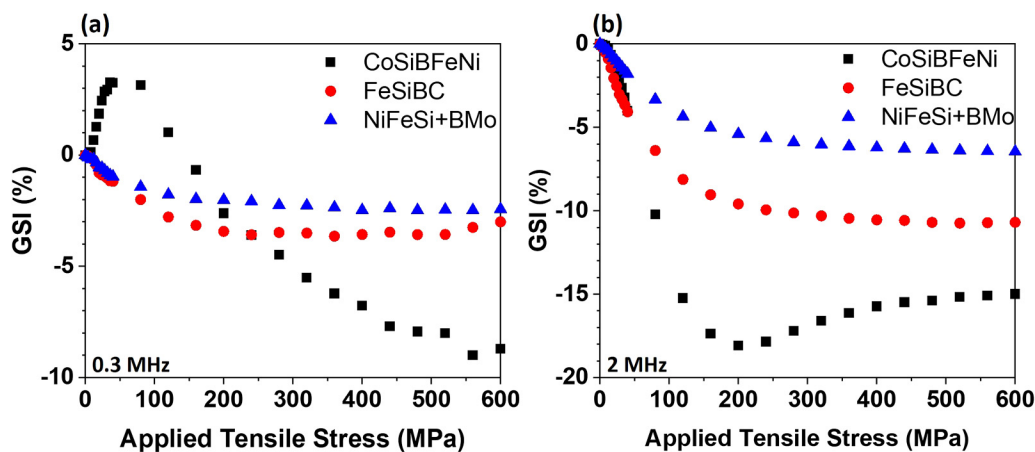


FIG. 6. Stress dependence of the GSI ratio of the Co-rich (black squares), Fe-rich (red circles), and Ni-rich (blue triangles) ribbons at $f=(a)$ 0.3 MHz and (b) 2 MHz.

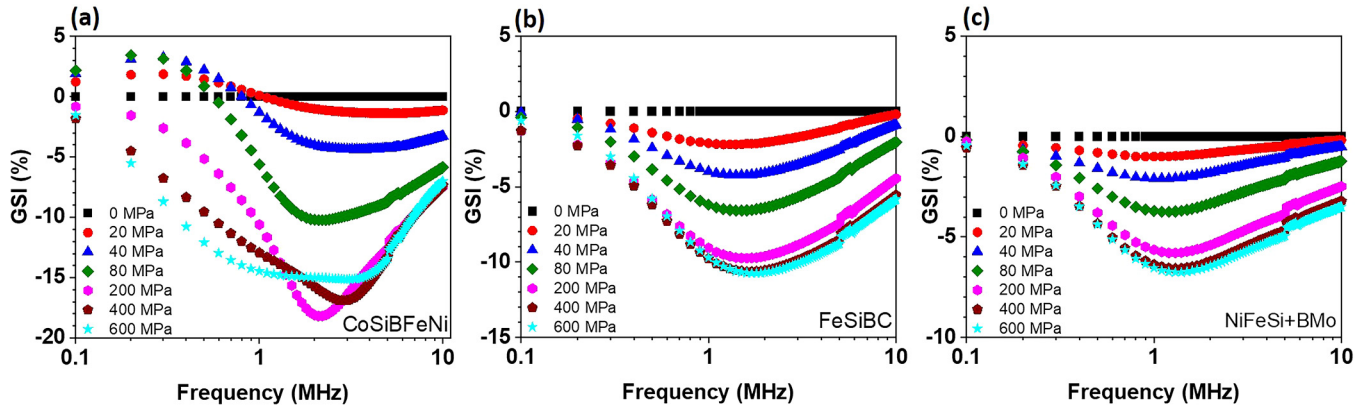


FIG. 7. Frequency dependence of GSI ratio for (a) Co-rich, (b) Fe-rich, and (c) Ni-rich ribbon samples under tensile stresses up to $\sigma = 600$ MPa.

in each sample. Thus, the materials with near-zero (or negative) λ_s coefficients exhibited larger peak GSI ratios than those with high λ_s .^{4,26–28} GSI curves for each material at their respective f_0 are shown in Fig. 8.

Figure 7 also further illustrates the frequency-dependent, non-monotonic GSI behaviors exhibited by the Co-rich ribbon. Behavior like those shown in Fig. 6(a), where positive GSI ratios were measured for low stresses before monotonically decreasing, was observed for $f < 1$ MHz. For $f > 1$ MHz, behaviors similar to those shown in Fig. 6(b) were observed, with the samples always exhibiting negative

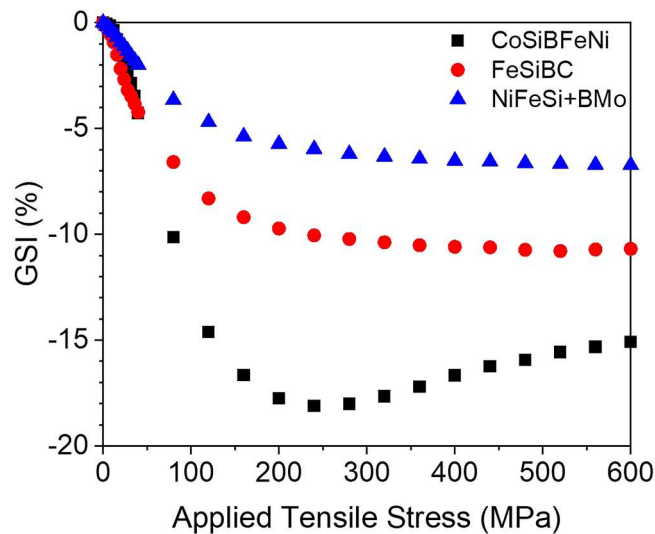


FIG. 8. Stress dependence of the GSI ratio measured for Co-rich (black squares), Fe-rich (red circles), and Ni-rich (blue triangles) ribbons. Each sample was measured from their respective critical frequency (f_0) (Co-rich sample $f_0 = 2.5$ MHz, Fe-rich and Ni-rich samples $f_0 = 1.5$ MHz).

GSI ratios which peaked between $\sigma = 200$ and 400 MPa and then began to decrease at higher stresses. The Fe- and Ni-rich samples exhibited simple, monotonic trends at all frequencies.

The differences in GSI behaviors between the materials implied that the transverse permeabilities of the samples responded differently to each other as the induced magnetoelastic anisotropies combined with other anisotropic energies terms. Typically, λ_s defines the domain structure of amorphous ribbons. Previous studies have generally found that ribbon samples with negative (or near-zero) λ_s coefficient have a greater tendency toward transverse-oriented domain structures than those with positive λ_s , which translates to materials with negative (or near-zero) λ_s coefficient having higher transverse permeability than those with positive λ_s coefficients.^{4,24,39,40} This clearly correlates with the data presented here, in Fig. 3 and Fig. 8, where the Co-rich samples displayed both higher peak GSI and GMI ratios than equivalent Fe- and Ni-rich ribbons. Furthermore, previous studies^{40–42} have shown a correlation between the size of a material's GSI response and the strength of its anisotropy field, with lower anisotropy fields resulting in higher GSI ratios. This suggests that, in the absence of induced stress, the Co-rich sample possessed a lower anisotropic field than Fe- and Ni-rich samples. However, in general, the anisotropy field was a combination of three effects: shape anisotropy and magnetocrystalline anisotropy, which were both fixed, and magnetoelastic anisotropy, which increased as stress was induced, potentially rotating the axis and modifying the strength of the net anisotropy of the samples.⁴³ Both rotations of anisotropy axis and modulations of the strength of the anisotropic field would be expected to intrinsically modify the transverse permeability and may have also modified the domain structure and magnetization dynamics exhibited by the ribbons, thus resulting in second order effects that further influenced the sample's transverse susceptibility.

Further complication was added by the facts that the magnetization dynamics contributing to the transverse permeability (i.e., domain wall motion and domain rotation) were likely to be affected differently by these changes and that the balance of those mechanisms would have been different at different frequencies, with

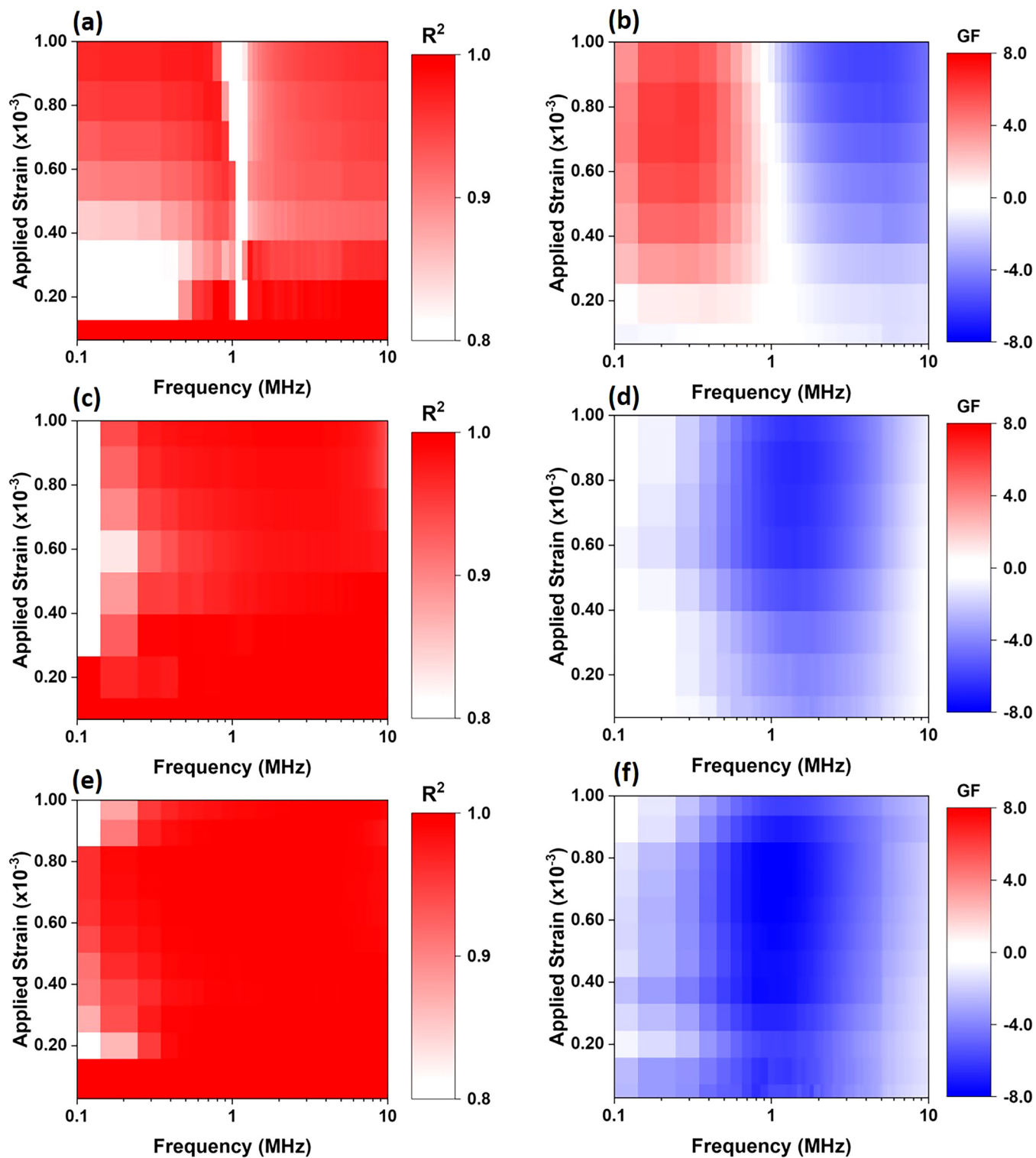


FIG. 9. Heatmaps of R^2 and gauge factors (GFs) for Co-rich ribbon [(a) and (b)], Fe-rich ribbon [(c) and (d)], and Ni-rich ribbon [(e) and (f)] for strains up to $\epsilon = 1 \times 10^{-3}$.

domain wall motion dominating at low frequencies and domain rotation progressively playing a more important role as frequency increased. As a result, the samples' GSI responses would not necessarily have been expected to be the same at all frequencies, potentially explaining the differing trends observed for the Co-rich sample at frequencies above and below $f = 1$ MHz. Untangling the details of these effects from our measurements is difficult, but the following is clear: For $f < 1$ MHz, the addition of small magnetoelastic anisotropies increased the transverse permeability (resulting in a positive GSI ratio) but decreased it at high stress/strains, thus resulting in the negative GSI ratios. In contrast to this, for $f > 1$ MHz frequency initial increases of stress/strain decreased the transverse permeability, while those over 200 MPa induced a modest recovery.

C. Optimization of samples strain performance

Having characterized the basic GSI characteristics of the three ribbon materials, we turned our attention to understanding how they could be best applied and optimized for strain sensing applications. Here, we split our analysis into two regimes: a low-strain regime ($\epsilon < 1 \times 10^{-3} / \sigma < 40$ MPa) and a high-strain regime ($\epsilon < 10 \times 10^{-3} / \sigma < 600$ MPa). We made this distinction semi-arbitrarily as it provided an interesting illustration of how different measurement tasks require different choices of material and measurement frequencies. As noted previously, we characterized a ribbons performance for any given maximum strain value within these ranges by the linearity of its response (as characterized by R^2) and the strength of the signal produced (as characterized by its GF) up to that value of the applied stimulus. These were also combined into a normalized FOM as an overall measure of applicability [Eq. (3)].

1. Low-strain sensor performance

Figure 9 presents the R^2 values and GFs as a function of frequency, for maximum strains within the low-strain regime, for all three materials. Here, the Co-rich sample exhibited a larger range of R^2 and $\Delta GSI / \Delta \epsilon$ values than the other materials, due to the non-monotonic GSI trends at low strains discussed previously. In

particular, the Co-rich sample exhibited highly non-linear behavior for strains lower than $\epsilon = 0.4 \times 10^{-3}$ at $f < 1$ MHz, and at all strains in the frequency window $f = 0.9$ – 1.2 MHz. Comparing the sample's R^2 plot with its GF plot explained the low R^2 values in these regions [Figs. 9(a) and 9(b)]. The low R^2 values for $f < 1$ MHz and maximum $\epsilon < 0.4 \times 10^{-3}$ were due to the initial lack of sensitivity to strain seen in the GF plot. Furthermore, the poor linearity seen in the 0.9–1.2 MHz range for all strain values was due to this region representing a boundary between frequencies that resulted in positive GSI ratios (highlighted red) to negative GSI ratios (highlighted blue) due to the two different non-monotonic behaviors discussed in Sec. III B.

While the Fe- and Ni-rich samples both showed poor linearity at frequencies below 0.3 MHz, they exhibited a consistently high R^2 value for all other frequencies, with linearity being particularly strong for Ni-rich ribbon [Figs. 9(e) and 9(f)]. The GF plots showed the Ni-rich sample to generally have higher GF than the Fe-rich sample, being consistently in the range -4.5% to -6% , at frequencies with peak sensitivity (0.6–2 MHz). In contrast, the GFs of the Fe-rich ribbons gradually increased from -3% to -6% in their own window of peak sensitivity (1–2 MHz), a fact that also explained these samples' slightly poorer linearity characteristics. The difference in GF values and linearity between the Ni- and Fe-rich samples was associated with the difference in their Young's modulus, E ; the modulus of the Ni-rich sample was more than twice that of the Fe-rich sample. This difference caused the Ni-rich sample to exhibit a lower strain for any given stress value, thus causing its GSI to vary more rapidly with strain.

Figure 10 presents FOM data for all three samples. As expected, the Co-rich sample performed worse than the other two samples with its highest FOM being ~ 0.55 , primarily because of the non-linearity of its response. The Fe- and Ni-rich samples both displayed higher performance, with the Ni-rich being well optimized to sense with good fidelity (FOM = 0.6–1) in the low-strain regime at around $f = 1$ MHz.

2. High-strain sensor performance

For the high stress/strain regime, all samples were subjected to a maximum tensile stress of $\sigma = 600$ MPa which translated to

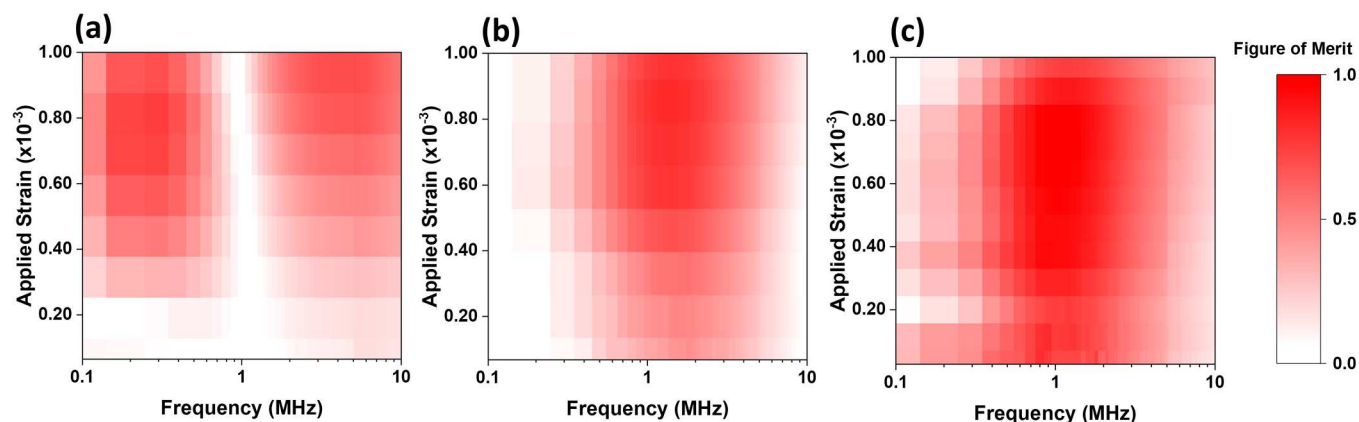


FIG. 10. Heatmap of figure of merit for (a) Co-rich, (b) Fe-rich, and (c) Ni-rich ribbons for strains up to $\epsilon = 1 \times 10^{-3}$.

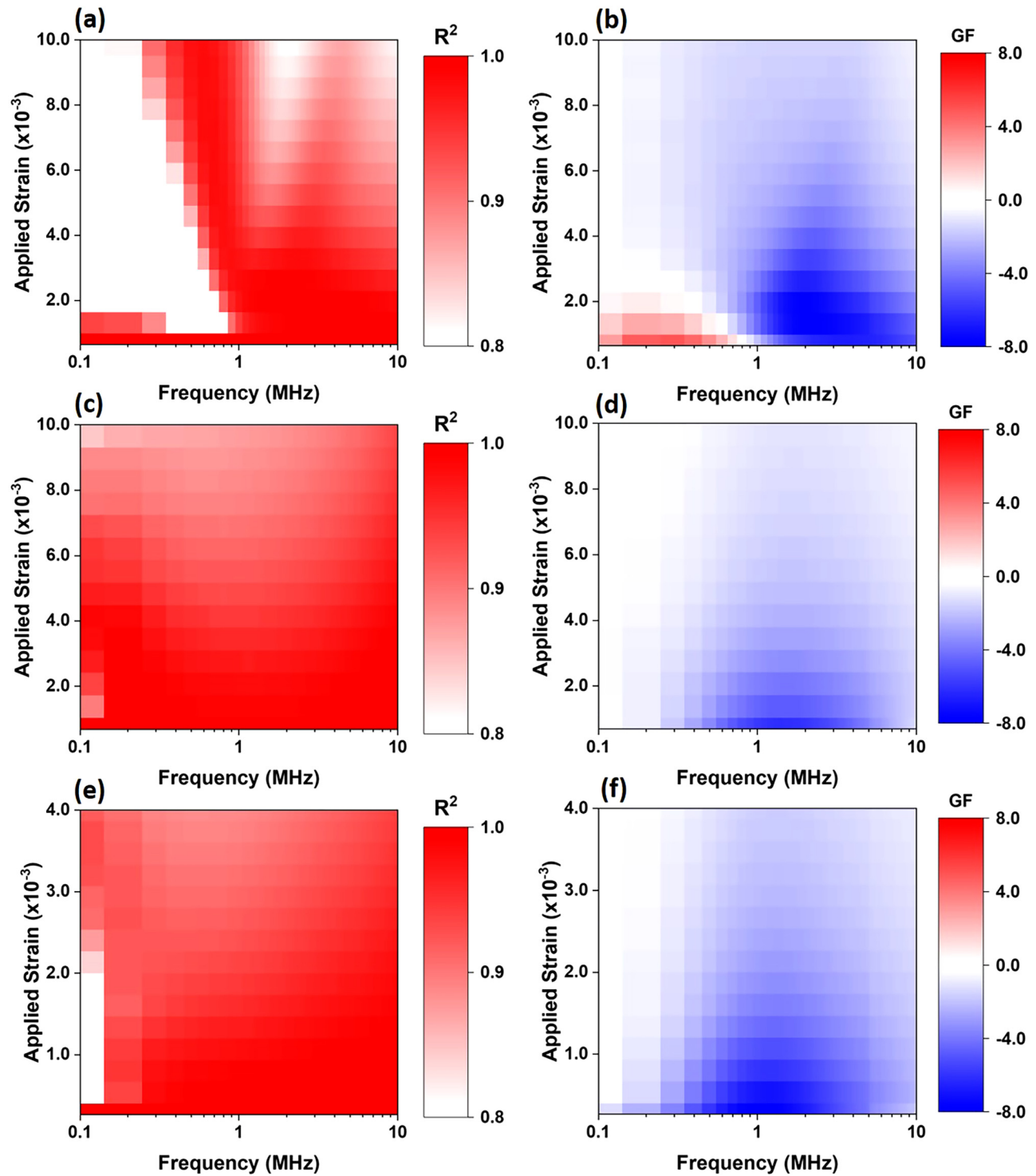


FIG. 11. Heatmaps of R^2 and gauge factors (GFs) for Co-rich ribbon [(a) and (b)], Fe-rich ribbon [(c) and (d)], and Ni-rich ribbon [(e) and (f)] for strains up to $\epsilon = 10 \times 10^{-3}$.

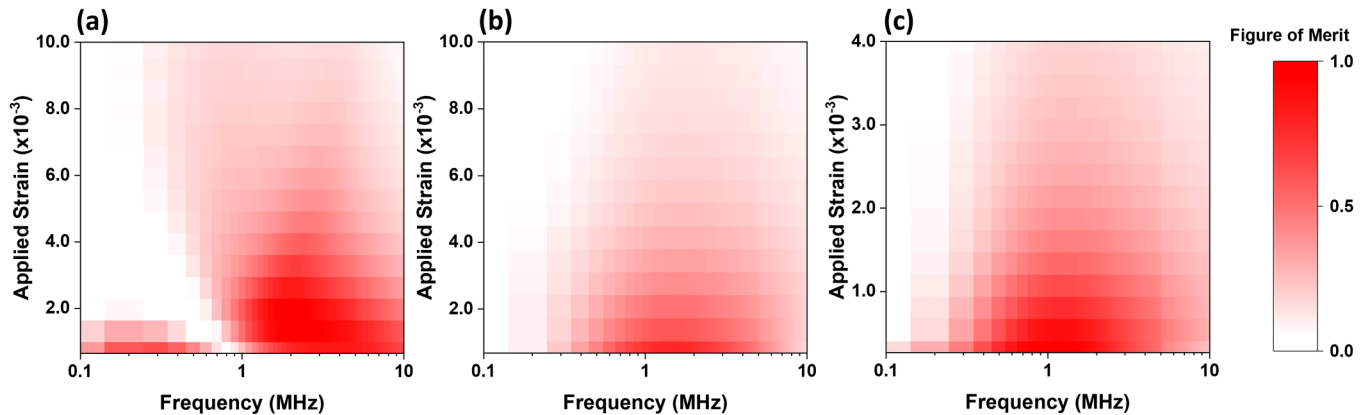


FIG. 12. Heatmap plots illustrating the figure of merit for (a) Co-rich, (b) Fe-rich, and (c) Ni-rich ribbon for strains up to $\varepsilon = 1 \times 10^{-3}$.

$\varepsilon = 10 \times 10^{-3}$ strain for Co- and Fe-rich samples due to their similar Young's moduli but a smaller strain of $\varepsilon = 4 \times 10^{-3}$ for the Ni-rich sample due to its higher Young's modulus.

Figure 11 presents the R^2 values and GFs as a function of frequency for maximum strains in the high-strain regime for all three materials. As in the low-strain regime, the Co-rich sample exhibited a larger range of R^2 values than the other two samples and was highly non-linear for $f < 1$ MHz for all values of maximum strain. This was caused by the low frequency, non-monotonic behavior discussed earlier, which can also be seen in the presence of both positive and negative in the GF plot at these frequencies. At higher frequencies, R^2 values increased and for $f > 1$ MHz, high linearity was observed up to $\varepsilon \sim 3 \times 10^{-3}$ with the material showing only negative GSI ratios. As the strain increased to values $\varepsilon > 4.0 \times 10^{-3}$, R^2 again decreased due to saturation of the GSI response and the onset of the high frequency non-monotonic behavior discussed previously. Fe- and Ni-rich samples exhibited relatively linear behaviors at low values of maximum strain but became less linear at high strains ($\varepsilon > 1.5 \times 10^{-3}$ for Fe-rich samples and $\varepsilon > 1.0 \times 10^{-3}$ for Ni-rich samples) due to the saturation of their GSI responses.

All three ribbons exhibited their greatest GF values for $f > 1$ MHz, with the Co-rich ribbon presenting the largest GFs due to its superior peak GSI ratio. Furthermore, the GFs for the Fe- and Ni-rich ribbons dropped rapidly with strain due to their larger λ_s values (and E in the case of Ni) causing saturation of their GSI response at lower strain. In contrast, for $f = 1\text{--}3$ MHz, the Co-rich sample retained high GF values up to $\varepsilon \sim 3 \times 10^{-3}$ as its lower λ_s led to a less rapid saturation of its GSI response.

Figure 12 presents FOM data for all three materials in the high-strain regime. Here, the Co-rich ribbon exhibited the best performance of all three materials, being able to detect strains up to 3×10^{-3} with good FOM, when working in the frequency range 2–3 MHz. As would be expected from the low-strain regime previously studied, the Fe-rich and Ni-rich samples initially showed good performance, but their FOM began to drop rapidly at $\varepsilon > 1 \times 10^{-3}$, respectively, due to saturation of their GSI response resulting in drops in R^2 , GF, and consequently FOM. None of the

ribbons were able to effectively act as sensors for strain beyond $\sim 3 \times 10^{-3}$ no matter what measurement frequency was selected.

The data presented above illustrate the complexity of selecting a material for a given strain sensing application. While one might naively argue that materials with large λ_s would be preferable, as these would maximize the size of induced magnetoelastic anisotropies, or that small λ_s would be preferable as this would maximize the broadly equivalent GMI effect and, thus, a sensor's dynamic range, the reality is much more complex and nuanced with differing magnetic and mechanical properties being optimal in different measurement regimes.

IV. CONCLUSION

In this study, we have explored the differences between the GMI and GSI behaviors of ribbons composed of three commercial amorphous materials ($\text{Co}_{66}\text{Si}_{15}\text{B}_{14}\text{Fe}_4\text{Ni}_1$, $\text{Fe}_{81}\text{B}_{13}\text{Si}_{3.5}\text{C}_2$, and $\text{Ni}_{40}\text{Fe}_{40}\text{Si} + \text{B}_{19}\text{Mo}_{1-2}$) under longitudinal tensile stresses up to $\sigma = 600$ MPa, equivalent to strains up to $\varepsilon = 10 \times 10^{-3}$. We have also assessed the linearity and gauge factor of the GSI effect in these materials in order to understand how they could be optimized for different strain sensing tasks.

We observed a simple relationship between a material's peak GMI and GSI ratios and the size of their saturation magnetostriction constants (λ_s) with the smaller values of λ_s producing the largest GMI and GSI responses. This occurred because ribbons with lower λ_s were magnetically softer and so exhibit higher maximum permeabilities, and thus a larger range of impedance values. While Fe-rich and Ni-rich samples always exhibited monotonic variations of impedance with applied stimuli, the Co-rich sample exhibited a variety of non-monotonic behaviors for both its GMI and GSI responses depending on the frequency and strain applied to the ribbons. We attributed these differing responses to the gradual transition from domain wall motion-based dynamics to domain rotation as the frequency increased and suggest that these mechanisms reacted differently to the shifting balance of magnetoelastic, magnetocrystalline, and shape anisotropies as the stress/

strain increased. Further study will be required to understand these effects in detail.

While the peak GSI ratio of the ribbons was easily understood, we observed that optimizing the response of the ribbons for strain sensing in different regimes was more complex. λ_s simultaneously determined the range of available impedances that a material could exhibit (i.e., a sensor's dynamic range), and in conjunction with the material's Young's modulus, E , the rate of their impedance changes with respect to stress/strain (i.e., sensitivity), and how quickly this saturated. These conflicting considerations meant that the optimal parameters for λ_s and E depended strongly on the range of strains to be sensed. In general, we observed that the Ni-rich ribbons, with modest λ_s with high E performed best in low-strain regimes, while Co-rich ribbons with near-zero λ_s and lower Young's modulus performed better in high-strain regimes. Fe-rich ribbons, which had the highest λ_s (and, therefore, hypothetically had the most stress sensitive magnetic properties), did not excel in either regime, but were broadly suitable for detecting low strains $\varepsilon < 1.5 \times 10^{-3}$. Our work indicates the challenge and complexity of optimizing the material properties of a GSI sensor for operation in any given stress/strain regime.

ACKNOWLEDGMENTS

The authors thank the Nuclear Decommissioning Authority (NDA) for funding this project.

AUTHOR DECLARATIONS

Conflict of Interest

The authors have no conflicts to disclose.

DATA AVAILABILITY

The data that support the findings of this study are available within the article.

REFERENCES

- ¹M. Kuźmiński, K. Nesteruk, and H. K. Lachowicz, "Magnetic field meter based on giant magnetoimpedance effect," *Sens. Actuators, A* **141**(1), 68–75 (2008).
- ²A. F. Cobeño, A. Zhukov, J. M. Blanco, V. Larin, and J. Gonzalez, "Magnetoelastic sensor based on GMI of amorphous microwire," *Sens. Actuators, A* **91**(1–2), 95–98 (2001).
- ³M. Knobel, M. Vázquez, and L. Kraus, "Giant magnetoimpedance," in *Handbook of Magnetic Materials* (Elsevier, 2003), Vol. 15, pp. 497–563.
- ⁴M. H. Phan and H. X. Peng, "Giant magnetoimpedance materials: Fundamentals and applications," *Prog. Mater. Sci.* **53**(2), 323–420 (2008).
- ⁵V. Zhukova *et al.*, "Effect of nanocrystallization on magnetic properties and GMI effect of Fe-rich microwires," *J. Electron. Mater.* **43**(12), 4540–4547 (2014).
- ⁶H. Q. Guo, H. Kronmüller, T. Dragon, Z. H. Cheng, and B. G. Shen, "Influence of nanocrystallization on the evolution of domain patterns and the magnetoimpedance effect in amorphous $\text{Fe}_{73.5}\text{Cu}_1\text{Nb}_3\text{Si}_{13.5}\text{B}_9$ ribbons," *J. Appl. Phys.* **89**(1), 514–520 (2001).
- ⁷Z. Lotfollahi, A. García-Arribas, A. Amirabadizadeh, I. Orue, and G. V. Kuryandskaya, "Comparative study of magnetic and magnetoimpedance properties of CoFeSiB-based amorphous ribbons of the same geometry with Mo or W additions," *J. Alloys Compd.* **693**, 767–776 (2017).
- ⁸T. Wang, Y. Zhou, C. Lei, J. Luo, S. Xie, and H. Pu, "Magnetic impedance biosensor: A review," *Biosens. Bioelectron.* **90**, 418–435 (2017).
- ⁹L. Chen *et al.*, "A prototype of giant magnetoimpedance-based biosensing system for targeted detection of gastric cancer cells," *Biosens. Bioelectron.* **26**(7), 3246–3253 (2011).
- ¹⁰G. V. Kuryandskaya, M. L. Sánchez, B. Hernando, V. M. Prida, P. Gorria, and M. Tejedor, "Giant-magnetoimpedance-based sensitive element as a model for biosensors," *Appl. Phys. Lett.* **82**(18), 3053–3055 (2003).
- ¹¹G. V. Kuryandskaya, V. Fal Miyar, A. Saad, E. Asua, and J. Rodriguez, "Giant magnetoimpedance: A label-free option for surface effect monitoring," *J. Appl. Phys.* **101**(5), 054505 (2007).
- ¹²J. Torrejón, L. Kraus, K. R. Pirota, G. Badini, and M. Vázquez, "Magnetostatic coupling in soft/hard biphasic magnetic systems based on amorphous alloys," *J. Appl. Phys.* **101**(9), 09N105 (2007).
- ¹³P. Corte-Leon *et al.*, "Engineering of magnetic properties and magnetoimpedance effect in Fe-rich microwires by reversible and irreversible stress-annealing anisotropy," *J. Alloys Compd.* **855**, 157460 (2021).
- ¹⁴F. Jin, L. Zhou, W. Cheng, Y. Zhang, B. Tong, and Y. Xu, "Effect of shape and annealing on the giant magnetoimpedance properties of FeCoSiB ribbon," *IEEE Trans. Magn.* **50**(10), 1–4 (2014).
- ¹⁵J. Nabias, A. Asfour, and J.-P. Yonnet, "The impact of bending stress on the performance of giant magneto-impedance (GMI) magnetic sensors," *Sensors* **17**(3), 640 (2017).
- ¹⁶J. Beato-Lopez, J. M. Algueta-Miguel, C. A. De La Cruz Blas, L. G. Santesteban, J. I. Perez-Landazabal, and C. Gomez-Polo, "GMI magnetoelastic sensor for measuring trunk diameter variations in plants," *IEEE Trans. Magn.* **53**(4), 1–5 (2017).
- ¹⁷L. P. Shen, T. Uchiyama, K. Mohri, E. Kita, and K. Bushida, "Sensitive stress-impedance micro sensor using amorphous magnetostrictive wire," *IEEE Trans. Magn.* **33**(5), 3355–3357 (1997).
- ¹⁸J. M. Blanco, A. Zhukov, and J. Gonzalez, "Effect of tensile and torsion on GMI in amorphous wire," *J. Magn. Magn. Mater.* **196–197**, 377–379 (1999).
- ¹⁹S. L. Zhang, J. F. Sun, D. W. Xing, F. X. Qin, and H. X. Peng, "Large GMI effect in Co-rich amorphous wire by tensile stress," *J. Magn. Magn. Mater.* **323**(23), 3018–3021 (2011).
- ²⁰L. De-Ren, L. Zhi-Chao, Z. Shao-Xiong, Z. Jun-Feng, L. Hui, and H. Wei, "Giant stress-impedance effect in amorphous and high-current-density electro-pulsing annealed $\text{Fe}_{73.5}\text{Cu}_1\text{Nb}_3\text{Si}_{13.5}\text{B}_9$ ribbons," *Chin. Phys. Lett.* **19**(7), 1000 (2002).
- ²¹F. X. Qin, H. X. Peng, V. V. Popov, and M. H. Phan, "Giant magnetoimpedance and stress-impedance effects of microwire composites for sensing applications," *Solid State Commun.* **151**(4), 293–296 (2011).
- ²²J. Beato-López, G. Vargas-Silva, J. I. Pérez-Landazábal, and C. Gómez-Polo, "Giant stress-impedance (GSI) sensor for diameter evaluation in cylindrical elements," *Sens. Actuators, A* **269**, 269–275 (2018).
- ²³J. Hu, H. Qin, J. Chen, and Y. Zhang, "Giant stress-impedance effect in $\text{Fe}_{73.5}\text{CuNb}_{3-x}\text{V}_x\text{Si}_{13.5}\text{B}_9$ amorphous ribbons," *J. Magn. Magn. Mater.* **266**(3), 290–295 (2003).
- ²⁴S. Dwevedi, G. Markandeyulu, P. R. Ohodnicki, A. Leary, and M. E. McHenry, "Stress-MI and domain studies in co-based nanocrystalline ribbons," *J. Magn. Magn. Mater.* **323**(15), 1929–1933 (2011).
- ²⁵P. Pan, R. D. Moorehead, and T. J. Hayward, "Influence of geometry on the giant magnetoimpedance of high-aspect ratio amorphous magnetic ribbons," *J. Appl. Phys.* **128**(17), 174504 (2020).
- ²⁶V. Raposo, J. I. Iniguez, D. Garcia, A. G. Flores, and M. Vazquez, "Internal magnetoimpedance of amorphous wires," in *Digest of INTERMAG 2003. International Magnetism Conference (Cat. No. 03CH37401)*, (2003), p. CB-05.
- ²⁷D. García, V. Raposo, O. Montero, and J. I. Iniguez, "Influence of magnetostriction constant on magnetoimpedance–frequency dependence," *Sens. Actuators, A* **129**(1–2), 227–230 (2006).
- ²⁸C. Morón, M. T. Carracedo, J. G. Zato, and A. García, "Stress and field dependence of the giant magnetoimpedance effect in Co-rich amorphous wires," *Sens. Actuators, A* **106**(1–3), 217–220 (2003).

- ²⁹See http://www.goodfellow.com/catalogue/GFCat4I.php?ewd_token=t5Hi55VEN7gmigQ8omoaE3EsYo1a6W&n=H8vrxrqtUtiolf3A3HDcEcWGNXdgOH&ewd_urlNo=GFCat4B11&Catite=CO810250&CatSearNum=5 for Cobalt/Silicon/Boron/Iron/Nickel Foil CO810250—Goodfellow Catalog (accessed 9 October 2019).
- ³⁰See http://www.goodfellow.com/catalogue/GFCat4I.php?ewd_token=t5Hi55VEN7gmigQ8omoaE3EsYo1a6W&n=H8vrxrqtUtiolf3A3HDcEcWGNXdgOH&ewd_urlNo=GFCat4B11&Catite=FE800250&CatSearNum=5 for Iron/Boron/Silicon Foil FE800250—Goodfellow Catalog (accessed 9 October 2019).
- ³¹See http://www.goodfellow.com/catalogue/GFCat4I.php?ewd_token=t5Hi55VEN7gmigQ8omoaE3EsYo1a6W&n=H8vrxrqtUtiolf3A3HDcEcWGNXdgOH&ewd_urlNo=GFCat4B11&Catite=NI800250&CatSearNum=5 for Nickel/Boron/Silicon Foil NI800250—Goodfellow Catalog (accessed 9 October 2019).
- ³²A. Zhukov *et al.*, “Manipulation of magnetic properties of glass-coated micro-wires by annealing,” *J. Magn. Magn. Mater.* **383**, 232–236 (2015).
- ³³A. Chaturvedi, T. Dhakal, S. Witanachchi, A.-T. Le, M.-H. Phan, and H. Srikanth, “Correlation between magnetic softness, sample surface and magnetoimpedance in $\text{Co}_{69}\text{Fe}_{4.5}\text{X}_{1.5}\text{Si}_{10}\text{B}_{15}$ ($X = \text{Ni}, \text{Al}, \text{Cr}$) amorphous ribbons,” *Phys. B: Condens. Matter* **405**(13), 2836–2839 (2010).
- ³⁴T. Eggers *et al.*, “Impact of the transverse magnetocrystalline anisotropy of a Co coating layer on the magnetoimpedance response of FeNi-rich nanocrystalline ribbon,” *J. Alloys Compd.* **741**, 1105–1111 (2018).
- ³⁵L. González-Legarreta *et al.*, “Magnetoimpedance dependence on width in $\text{Co}_{66.5}\text{Fe}_{3.5}\text{Si}_{12.0}\text{B}_{18.0}$ amorphous alloy ribbons,” *J. Appl. Phys.* **113**(5), 053905 (2013).
- ³⁶C. Zhao, X. Zhang, Q. Liu, and J. Wang, “GMI field sensitivity near a zero external field in Co-based amorphous alloy ribbons: Experiments and model,” *J. Phys. D: Appl. Phys.* **49**(6), 065006 (2016).
- ³⁷Y.-H. Ding, K. Xue, W.-Y. Wang, and X. Ma, “Influence of aspect ratio on giant magnetoimpedance effect for $\text{Fe}_{77}\text{Co}_{18}\text{Si}_{11}\text{B}_4$ amorphous ribbons,” *Acta Metall. Sin. (Engl. Lett.)* **30**(12), 1236–1242 (2017).
- ³⁸J. Hu, H. Qin, J. Chen, and Y. Zhang, “Giant stress-impedance effect in $\text{Fe}_{73.5}\text{CuNb}_{3-x}\text{V}_x\text{Si}_{13.5}\text{B}_9$ amorphous ribbons,” *J. Magn. Magn. Mater.* **266**(3), 290–295 (2003).
- ³⁹M. H. Phan, H. X. Peng, M. R. Wisnom, S. C. Yu, C. G. Kim, and N. H. Nghi, “Effect of annealing temperature on permeability and giant magneto-impedance of Fe-based amorphous ribbon,” *Sens. Actuators, A* **129**(1–2), 62–65 (2006).
- ⁴⁰D. Li, Z. Lu, and S. Zhou, “Induced magnetic anisotropy and stress-impedance effect in nanocrystalline $\text{Fe}_{73.5}\text{Cu}_1\text{Nb}_3\text{Si}_{13.5}\text{B}_9$ ribbons,” *IEEE Sens. J.* **6**(4), 924–927 (2006).
- ⁴¹S. Mansourian, A. Bakhshayeshi, and R. Taghavi Mendi, “Giant magneto-impedance variation in amorphous CoFeSiB ribbons as a function of tensile stress and frequency,” *Phys. Lett. A* **384**(26), 126657 (2020).
- ⁴²D. R. Li, Z. C. Lu, and S. X. Zhou, “Magnetic anisotropy and stress-impedance effect in Joule heated $\text{Fe}_{73.5}\text{Cu}_1\text{Nb}_3\text{Si}_{13.5}\text{B}_9$ ribbons,” *J. Appl. Phys.* **95**(1), 204–207 (2004).
- ⁴³Z. Guo *et al.*, “Electric field induced non-90° rotation of the easy axis of a ferromagnetic film,” *Appl. Phys. Lett.* **112**(5), 052904 (2018).